

ENERGY DISSIPATION OF THIN-WALLED RIBBED SPHERES FOR CARGO AIRDROP

Andrew Lloyd[1], Prof KC Wong[2]

[1]PhD candidate at The University of Sydney
[2]The University of Sydney

Abstract

Cargo airdrop has relied on cardboard honeycomb Energy Dissipating Material (EDM) for half a century. The material is logistically inefficient, transmits a high initiation peak before its crush plateaus, and only about 70% of stack height contributes before densification. This paper presents an additively manufactured alternative: a thin-walled sphere whose load-bearing shell is an open lattice of ribs, printed in Tough 1500 stereolithography resin. A concentric two-sphere configuration predicted by finite element analysis to extend crush duration is empirically rejected: the curved sphere-on-sphere interface destroys the rolling hinge. The revised crush response resolves into three modes — pole flattening, a velocity-invariant rolling-hinge backbone, and velocity-dependent densification. Drop tower testing demonstrates that a single thin-walled sphere produces a smooth force-time profile with no initial peak and a sustained plateau at a relatively constant force, as the rolling hinge travels around the shell — the backbone obeys Updike's radius-independent $\sqrt{\delta}$ law. Velocity sweeps show the dissipation is rate-independent structural hysteresis, with specific damping capacity rising to approximately 0.9 near the densification limit, so a single force-displacement backbone predicts the full impact envelope. Implications for a graded sphere arrays synthesising a pseudo-plateau are considered.

Keywords: airdrop, energy absorption, thin-walled sphere, ribbed shell, impact

1. Introduction

Conventional airdrop delivers cargo under unguided parachutes. A minimum drop height ensures the canopy fully deploys and reaches steady descent before a predominantly vertical surface impact; the faster the load falls, the more accurate the delivery, but the more severe the dynamic loading the cargo must survive. Recent humanitarian airdrops in Gaza and the resupply of Tristan da Cunha confirm the method's continuing relevance where other supply means are restricted.

Impact energy is absorbed universally by a cardboard honeycomb Energy Dissipating Material (EDM) [1]. Its 2.5-dimensional geometry — honeycomb cells in the transverse plane, uniform in the loading direction — produces a high initial peak force followed by a near-constant dynamic crush stress until densification occurs, once the stack has crushed to around 30 percent of its original height [2]. Figure 1 shows the Australian Container Delivery System (CDS): the EDM is contained between the skidboard that interfaces with the aircraft cargo handling system and the plywood board that secures the cargo [3]. More EDM stacks absorb more energy but raise the likelihood of toppling at impact and consume cargo height under aircraft limits; there is consequently more space available for energy-dissipating structures in the transverse direction than in the direction of crush.



Figure 1 – Container Delivery System [3]

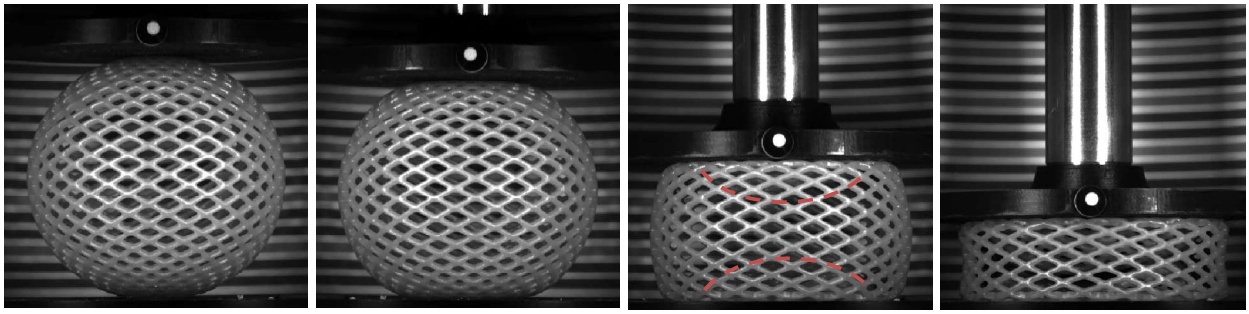
EDM sizing is iterative: the g-loading on impact is directly proportional to EDM surface area and payload mass, and the stroke to velocity squared [3]. The area is set by the g-limit, the available stroke is checked against densification, and a safety factor of 1.5 covers the initiation peak and oblique loading. Three limitations motivate this work: the material is logistically inefficient (a large-volume, low-mass product pre-positioned at the expense of cargo space); its crush efficiency (average over peak load) is limited by the initiation peak; and only about 70% of the stack height contributes to energy absorption before bottoming out.

Additive manufacturing admits geometry unavailable to conventional processes. A thin-walled sphere embraces deformation in the transverse direction — a meridional progression — in which the rounded contact produces a slow onset of force, avoiding the initiation peak of biased structures, while a travelling hinge sustains the crush force. The authors originally proposed concentric spheres [4] to extend the crush duration; the empirical testing reported here does not reproduce the simulated benefit, and the single-wall sphere, tuned through its lightening rib pattern, is now the focus. The paper characterises the single-wall ribbed sphere experimentally (Sections 3–4), develops a calibrated analytical model (Section 5), quantifies its damping mechanism (Section 6) and assesses its prospects against EDM (Section 7).

2. Ribbed Thin-Walled Spheres as Energy Dissipators

2.1 Crush Mechanism

Compressed between flat platens, a thin-walled spherical shell deforms in three stages (Figure 2): flattening at the contact patch (b), inward dimpling of the poles with a circular travelling hinge propagating from the dimple boundary toward the equator (c, red dashed lines), and buckling at the equator (d). Updike [5] showed the load-deformation relation of the plastic hinge to be largely independent of the shell radius, governed instead by wall thickness and material yield; De'Oliveira and Wierzbicki [6] demonstrated that the rolling hinge remains valid for crush distances approaching the shell radius; and Calladine [7] generalised the travelling hinge as a recurring feature of large plastic deformation in shells. The practical consequence is a long stroke at near-constant force, without the discrete buckling events that characterise honeycomb collapse. Gupta [8] reported that the quasi-static deformation modes of spherical domes are preserved at impact velocities up to 9 m/s, with modest strain-rate sensitivity in metallic shells. This work exploits the same geometric mechanism in an additively manufactured polymer shell whose wall is locally graded by a lightening rib pattern.



(a) (b) (c) (d)

Figure 2 – Mechanisms of crush: (a) initial loading; (b) contact flattening; (c) travelling hinge; (d) equatorial buckling

2.2 Lattice Geometry

The test articles are 60 mm outer-diameter spheres carrying a surface lattice generated with the rib function in nTopTM. A U–V grid (U = V = 20) places 20 ribs along lines of longitude and 20 around lines of latitude; the cells they bound are open, so the ribs themselves form the entire load-bearing shell. Two parameters define the lattice (Figure 3): the wall thickness (wt), the depth of the rib in the shell-normal direction, and the rib thickness (rt), the width of the rib in-plane. The wall thickness enters the plastic moment of each rib through a squared dependence while the rib thickness enters linearly, decoupling the lattice's bending stiffness from its mass — a design space unavailable in conventional EDM and the one explored here.

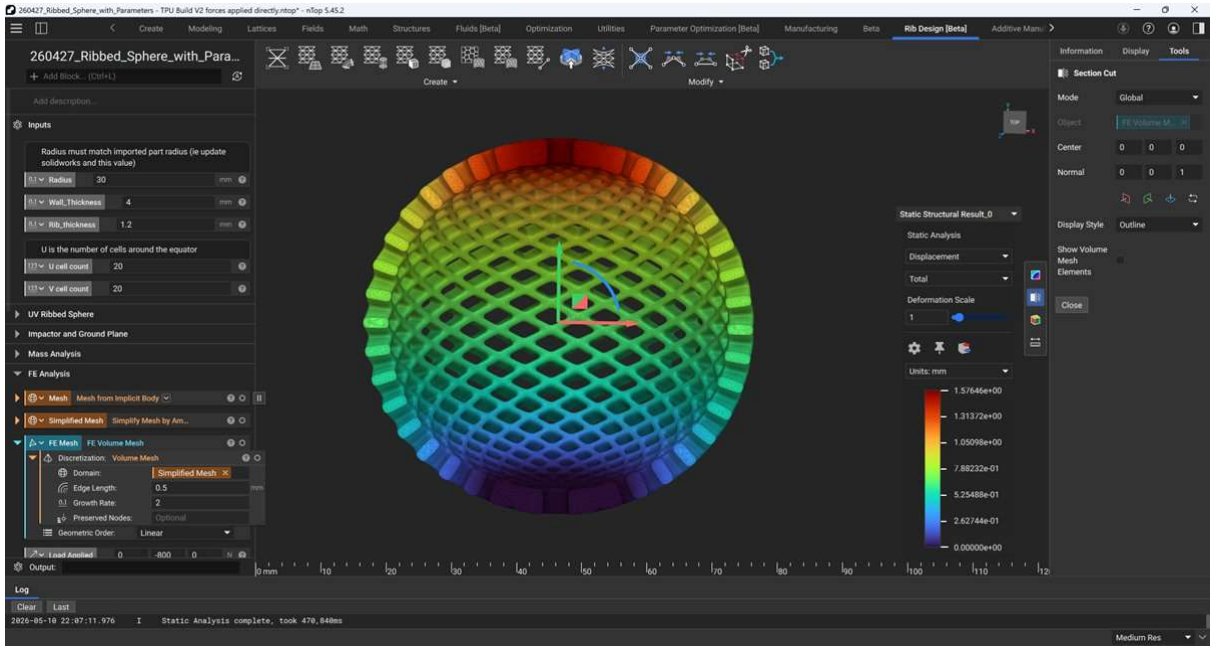


Figure 3 – Unit-cell geometry modelled in nTop

2.3 Fracture-Informed Design

An open rib lattice was selected over a continuous shell because three mechanisms conspire to make a continuous photopolymer sphere fracture-critical under airdrop impact: the intrinsic brittleness of the crosslinked network, the thickness-driven transition to plane strain fracture, and the strain-rate-driven ductile-to-brittle transition.

Stereolithography resins are thermosets cured by radical photopolymerisation of multifunctional acrylate and methacrylate monomers. The crosslink density that provides stiffness simultaneously limits fracture toughness — brittleness and poor impact resistance are recognised as principal drawbacks of photocurable acrylate systems [10] — because restricted molecular mobility at a crack tip shrinks the plastic zone available to arrest propagation. Idrees et al. [11] demonstrated this stiffness-toughness trade-off directly for Stereolithography (SLA) vat photopolymerisation systems.

For a low-toughness material, the crack-tip stress state is governed by section thickness. Thin sections deform under plane stress, sustaining a large, energy-dissipating plastic zone; thicker sections constrain lateral deformation into a triaxial plane strain state in which the plastic zone collapses, the apparent toughness falls to its minimum value K_{Ic}, and fracture is rapid and brittle [12]. Plane strain dominates when

$$B \geq 2.5 \cdot (K_{Ic} / \sigma_y)^2 \quad (1)$$

where B is the section thickness, K_{Ic} the plane-strain fracture toughness and σ_y the yield strength [12]. For SLA acrylates K_{Ic} lies broadly in the range of 0.7–1.0 MPa·m½ [13, 14]; with the Tough 1500 V1 tensile yield of approximately 33 MPa, the critical thickness is approximately 1.1–2.3 mm, with a mid-range estimate around 1.7 mm. A continuous shell at the 3–4 mm walls used in this study would therefore sit on or beyond the plane strain boundary. Quagliato et al. [15] confirmed the thickness dependence experimentally for SLA acrylates, with thicker sections more susceptible to brittle failure under dynamic load.

Strain rate drives the third mechanism: above a ductile-to-brittle transition rate, molecular chain mobility cannot sustain crack-tip plasticity regardless of thickness [16], while the apparent modulus and yield strength rise and the elongation at break falls sharply [16, 17]. For the tested environment — impacts of 1.5–5.5 m/s, crush events of 8–20 ms and ribs of 0.8–1.6 mm width bent through large angles — rib strain rates are estimated at 33–200 s^{-1}, firmly in the regime where rate stiffening is significant and the ductile-brittle boundary is approached for a continuous shell of comparable thickness.

The lattice mitigates all three mechanisms with no change of material. The rib width (0.8–1.6 mm) lies below the mid-range critical thickness, keeping each rib in plane stress; the open cells remove the geometric continuity a crack requires, each rib intersection acting as a crack-arrest feature; and the rolling hinge works the ribs in bending through progressive joint rotation rather than driving them to tensile failure. Cracking is nonetheless observed in practice but is almost always arrested by the lattice (Section 4.3); the catastrophic exception — the stiffest 1.6 mm rib / 3 mm (UV_F) wall article — marks the practical upper bound of the rib-stiffening strategy. Tough 1500 V1 was selected as the stiffest resin expected to remain in the ductile, crack-arresting regime at these rib dimensions and strain rates; stiffer resins would raise the plateau force at the cost of toughness and a narrower plane stress window.

3. Experimental Method

3.1 Test Articles

Test articles were produced on a Formlabs Form 3+ in Tough 1500 V1 resin. Professional stereolithography provides near-isotropic material properties, removing inter-layer failure as a confounding variable; the fracture rationale for the ribbed geometry is given in Section 2.3. Table 1 catalogues the articles. Designations are suffixed with a number where multiples were manufactured; repeat drops on the same article were compared to confirm a purely elastic impact, and any permanent axial deformation was measured and recorded before further testing.

Printed articles were hand-washed in IPA for 10 minutes on the raft, washed a further 10 minutes in a FormWash, dried with compressed air and cured in a FormCure on the Tough 1500 V1 setting before being twisted off the raft. All measured 59.95 mm pole-to-pole and 60.00 mm across the equator. EDM specimens were cut to 60 mm squares on an Epilog CO2 laser to ensure accuracy.

Test Article Designation	Type	Height (mm)	Width (mm)	Depth (mm)	rt1 (mm)	wt1 (mm)	rt2 (mm)	wt2 (mm)
E	EDM	76.2	60	60				
UV_Z	UV_20_20	60	60	60	1.2	2		
UV_A	UV_20_20	60	60	60	1.2	3		
CUV_A	UV_20_20	60	60	60	1.2	2.25	0.6	1.5
UV_B	UV_20_20	60	60	60	0.8	2		
CUV_B	UV_20_20	60	60	60	0.8	2.25	0.4	1.5
UV_C	UV_20_20	60	60	60	0.8	3		
CUV_C	UV_20_20	60	60	60	0.8	3	0.4	2
UV_D	UV_20_20	60	60	60	1.2	4		
UV_E	UV_20_20	60	60	60	1.6	2		
UV_F	UV_20_20	60	60	60	1.6	3		

Table 1: Test Articles

3.2 Instrumentation

Figure 4 shows representative test articles and Figure 5 the experimental arrangement, comprising:

- Instron 9450 Drop Tower with High Energy System and a M3962 Force Transducer (1MHz for 60ms or 0.5MHz for 120ms)
- Photron Fastcam Mini AX50 High Speed Camera (9000fps 512x384 pixels or 10000fps 384x384 pixels)
- Micro-Epsilon optoNCDT 2300-50 (20kHz 0.8µm)
- Custom made 80mm diameter, 8mm thick impactor (constructed from Ultimaker Polycarbonate)

Most force records used 1 MHz; the Instron-triggered camera used the wider frame for EDM and the tighter frame for the spheres, and the manually started laser records were aligned in MATLAB by thresholding above the sensor noise ceiling.



Figure 4 – Test Articles



Figure 5 – Experimental Equipment

3.3 EDM Baseline

Seventeen 60 × 60 mm EDM articles were tested at a drop mass of 5.4 kg — an expected g-loading of 30G with the 1.5 safety factor applied — across 2.5–5.5 m/s (Figure 6). The expected high initial peak followed by localised buckling at a constant dynamic crush stress is observed. Densification, anticipated between 4.5 and 5.0 m/s, extended to 5.2 m/s in testing, with the 5.5 m/s result fully densified; an additional layer is required once this capacity is consumed. Peak forces are similar up to 4.5 m/s while the plateau duration grows with velocity. The reduced plateau capacity at 5.2 and 5.5 m/s is attributed, from high-speed footage, to inertia-driven global buckling of the stack (between 2.5 and 15 ms in the 5.5 m/s case); Figure 7 contrasts the localised and global modes.

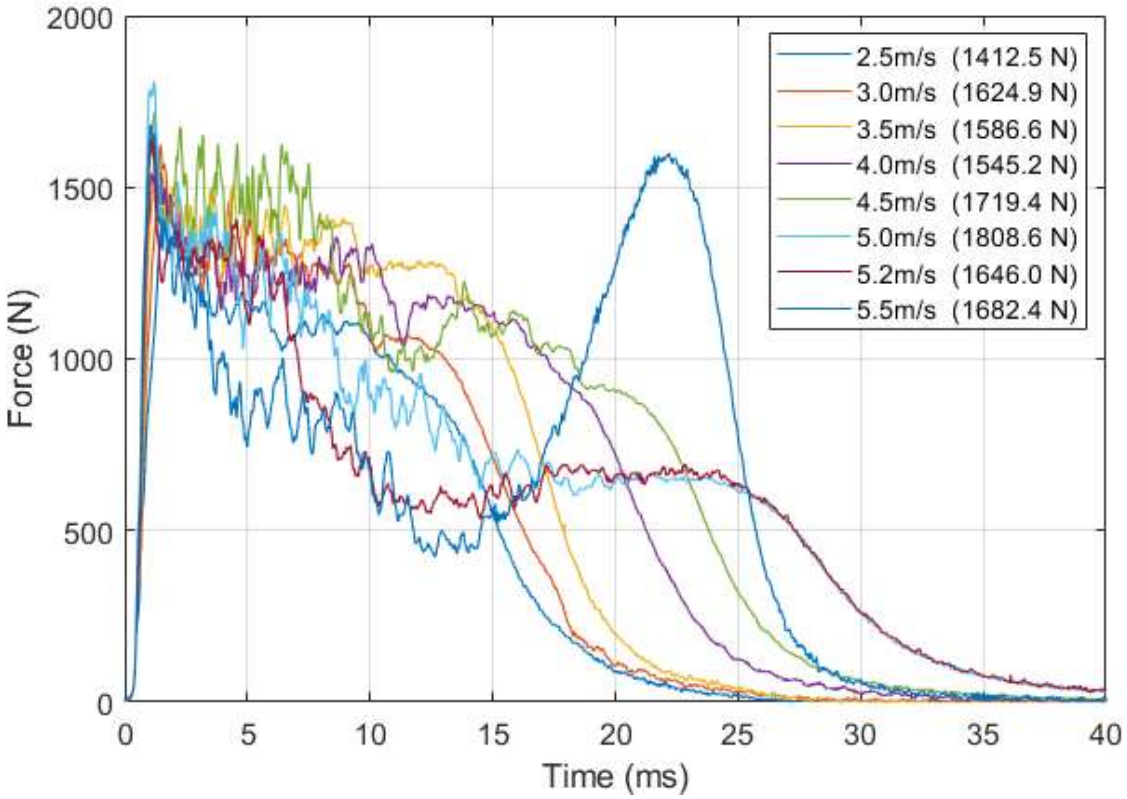


Figure 6 – EDM Baseline



Figure 7 – EDM buckling modes: localised at 4 m/s (left); global at 5 m/s (right)

4. Results

4.1 Concentric Spheres –Departure from FEA

The concentric sphere was modelled in LS-DYNA™ [4] as a means of extending crush duration: the inner sphere was to engage as the outer sphere's force contribution decayed, flattening and lengthening the force-time profile. Empirical testing did not reproduce the benefit. In Figure 8 the three concentric traces (2.25 mm outer wall, 1.5 mm inner wall, diamond markers) show the expected lower initial force from the thinner outer wall, but an unexpected, substantially higher second peak; the articles were heavily densified at 3.0 m/s and bottomed out beyond. Equally unexpected was the clean force plateau of the single-wall traces at 2.0 and 2.5 m/s — the travelling hinge of Section 2.1 supplying an idealised dissipator without any internal geometry.

The hypothesised mechanism is the sphere-on-sphere interface. The rolling hinge requires a flat reaction surface; once the outer sphere's contact zone has inverted, the inner sphere loads against an inverted dome — a curved-on-curved contact that reinforces the structure into a torus and initiates densification. The design strategy is therefore redirected: the tuned single-wall sphere is the unit cell, and crush duration is extended at array level by stacking layers separated by interlayer plates that restore a flat reaction surface to each layer.

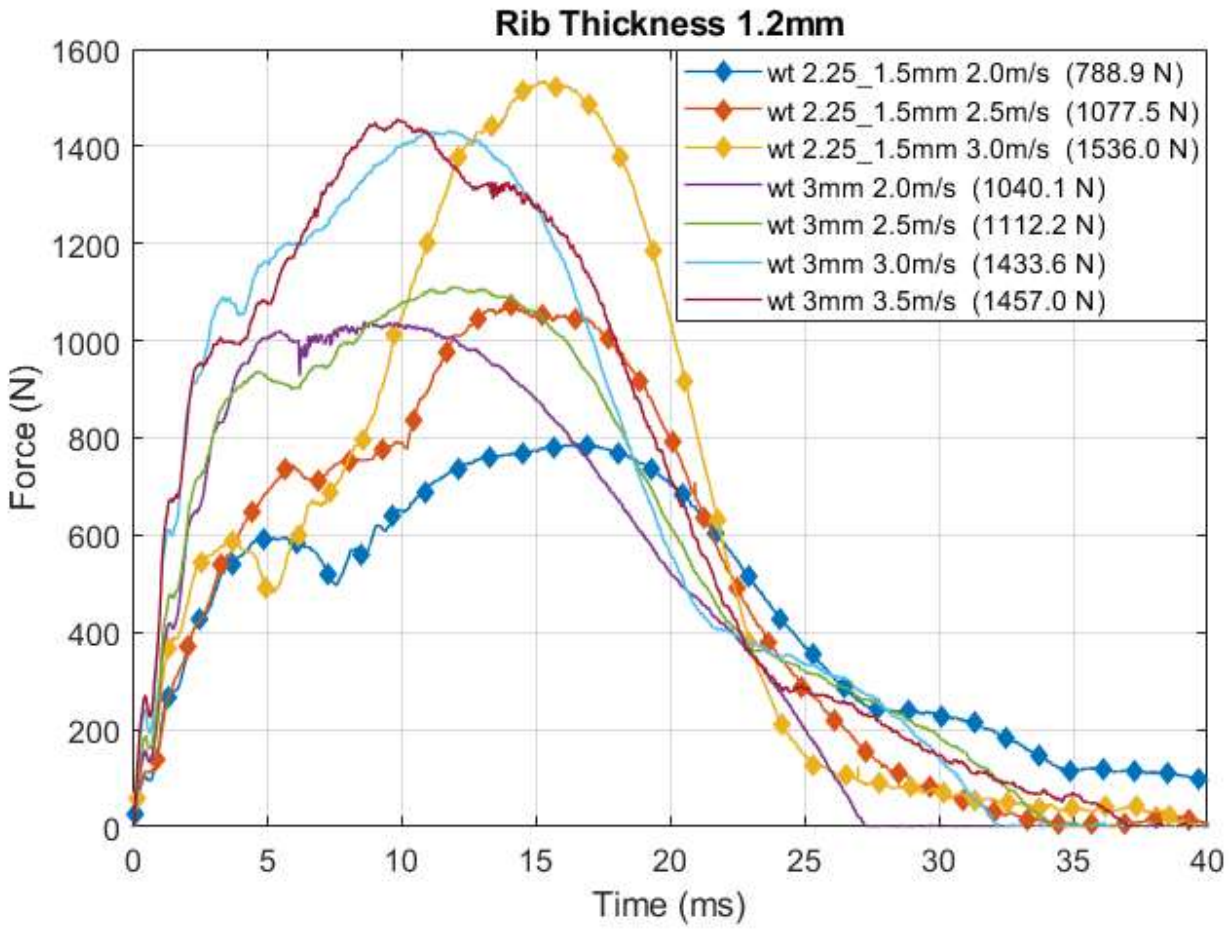


Figure 8 – Comparison of Concentric Spheres and Single Walled Spheres

4.2 Single-Wall Sphere versus EDM

Figure 9 compares a 60 × 60 mm EDM specimen with a 60 mm single-wall sphere (3 mm wall, 1.2 mm rib) at the common 5.4 kg drop mass used across all tests reported. The EDM trace shows the sharp initiation peak of cell-wall buckling followed by an oscillating plateau of sequential cell collapse. The sphere shows a markedly different profile: an initiation phase as the contact patch flattens and the hinge forms, a sustained plateau at near-constant force as the rolling hinge travels around the shell, and a roll-off as the impactor comes to rest. Its peak force is comparable to the EDM plateau but is reached without the impulsive spike: with no buckling event to overcome at initiation, the crush efficiency (mean over peak force) matches EDM without the jerk. This is the primary motivation for pursuing the geometry for cargo airdrop.

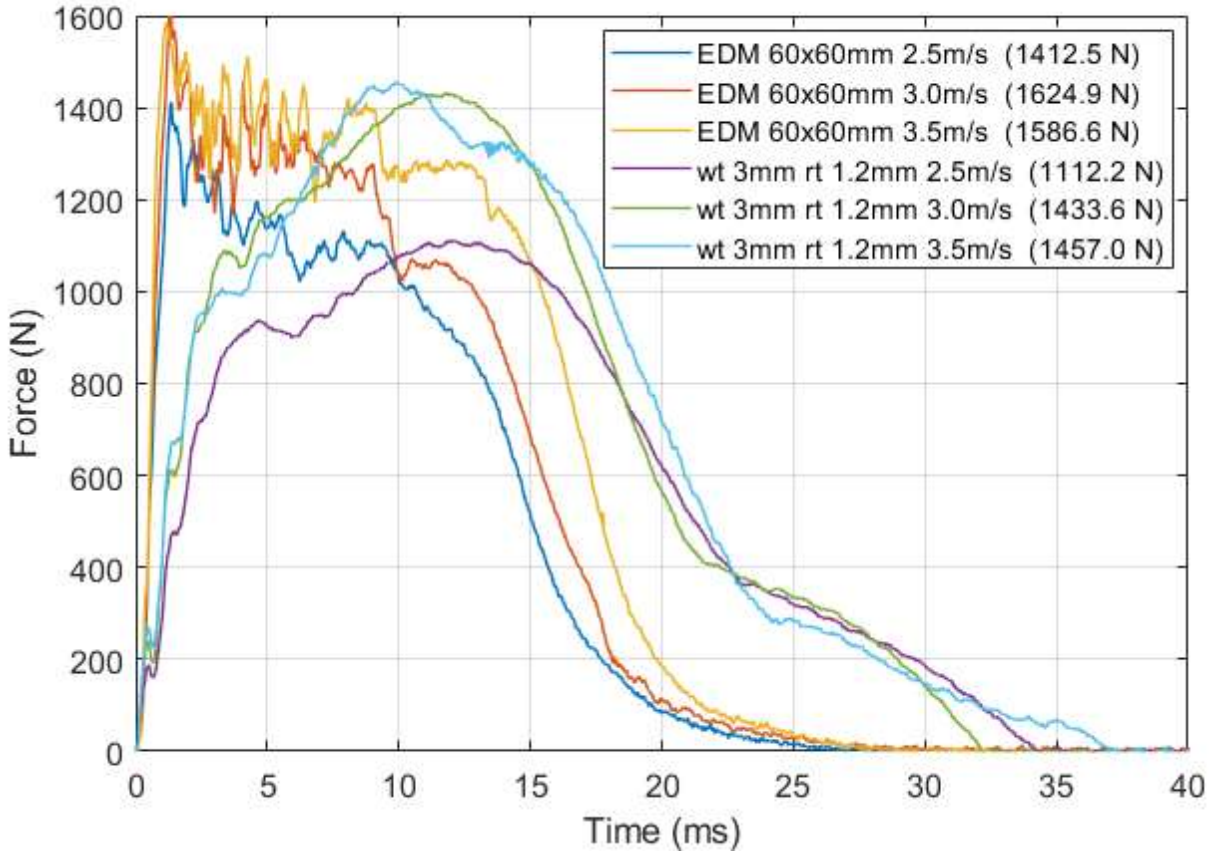


Figure 9 – EDM baseline compared to single-walled sphere

4.3 Velocity Sweeps and Failure Modes

The plateau forces summarised in Section 5.4 are drawn from the individual velocity sweeps of each geometry. These sweeps are presented in Figures 10 to 13 and show the full force-time behaviour from the lowest tested velocity up to the onset of densification or article failure. They also show the cracking behaviour of the ribbed structure, which is central to the fracture argument of Section 2.3.

Four geometries were swept to densification — 1.2 mm ribs on 3 and 4 mm walls, and 1.6 mm ribs on 2 and 3 mm walls; a 0.8 mm rib series was discarded, the displacements needed to reach peak force having tripped the Instron bump stops.

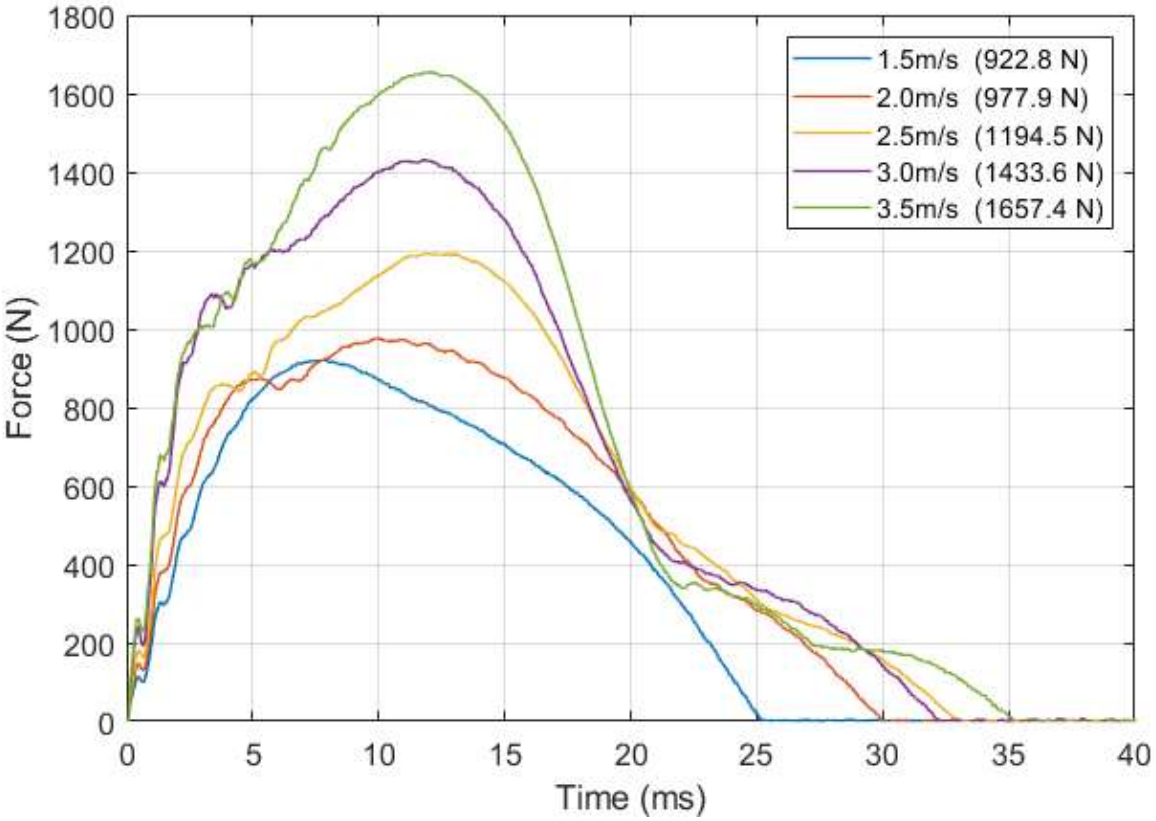


Figure 10 – Velocity sweep for the 1.2 mm rib / 3.0 mm wall geometry (UV_A)

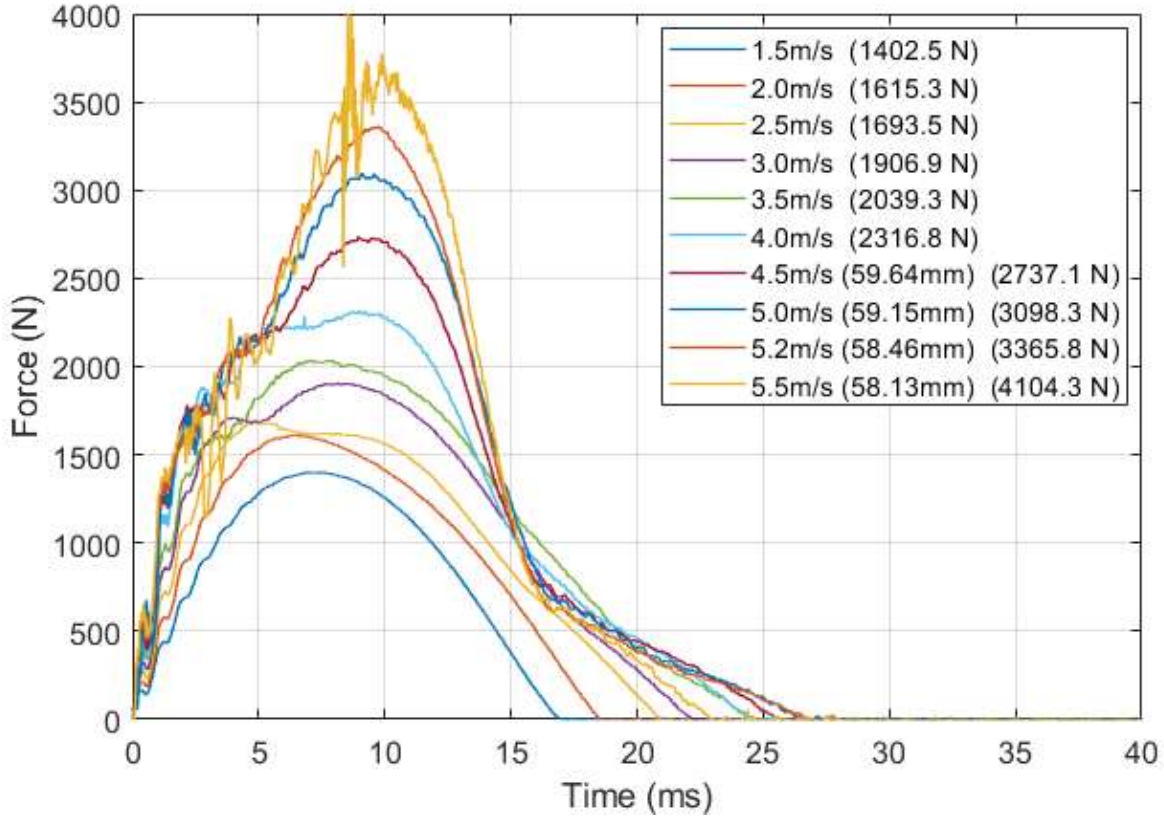


Figure 11 – Velocity sweep for the 1.2 mm rib / 4.0 mm wall geometry (UV_D), articles with a dimensional parenthesis were pre-strained

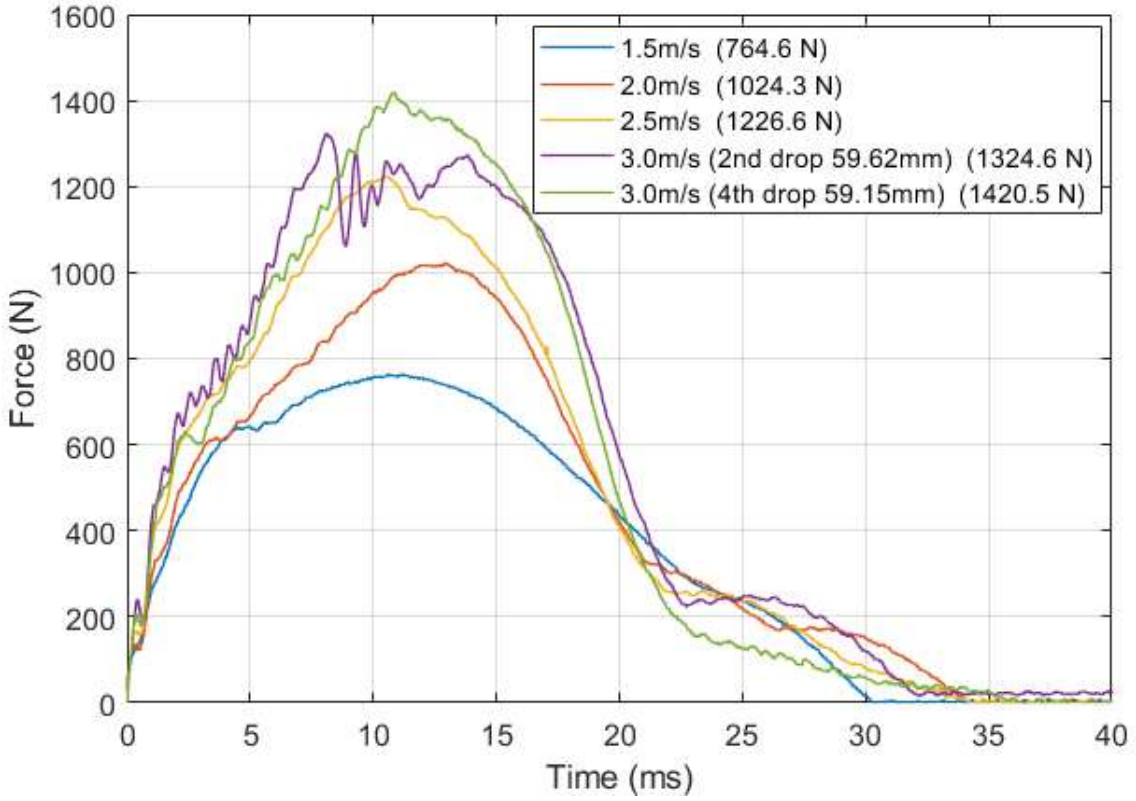


Figure 12 – Velocity sweep for the 1.6 mm rib / 2.0 mm wall geometry (UV_E), articles with a dimensional parenthesis were pre-strained

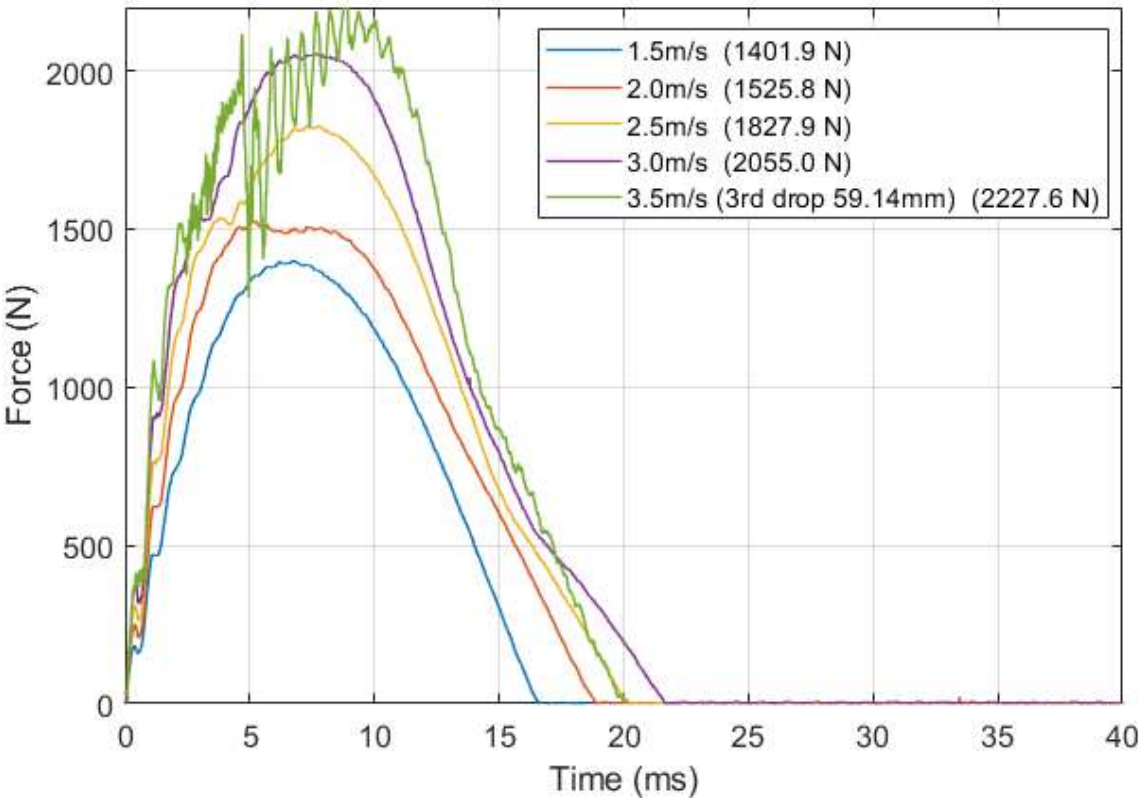


Figure 13 – Velocity sweep for the 1.6 mm rib / 3.0 mm wall geometry (UV_F), articles with a dimensional parenthesis were pre-strained

Cracking was observed across the test programme but was, in the great majority of cases, contained by the lattice. Within the valid velocity range, isolated ribs cracked sporadically on some articles, typically only one or two ribs per article. Where these events were captured rather than excluded from the dataset, they appear as high-frequency noise superimposed on the smooth plateau. The noise is the mechanical signature of individual rib failures; because each rib intersection acts as a crack arrest feature, these failures did not propagate and the surrounding ribs continued to carry load, preserving the plateau. The majority of articles that exhibited more than incidental cracking, at increased velocity, were excluded from the quantitative dataset to avoid biasing the plateau force readings.

At velocities beyond the valid range — where the result was no longer a clean rolling hinge event — the dominant end-of-life failure mode was cracking that initiated at the top pole of the sphere, the point of highest curvature and the location where the contact and inertial stresses concentrate as the hinge completes its travel. In most articles this pole crack arrested at the first rib it encountered, once again demonstrating the containment provided by the open-cell lattice. The structure was typically left with a single cracked rib at the pole rather than a propagating split.

The exception was the 1.6 mm rib / 3 mm wall geometry, the stiffest tested: a fresh article at 3.5 m/s failed catastrophically, a single crack propagating as a split along the full length of the sphere (the 3.5 m/s trace in Figure 13 is from a different, pre-strained article that did not fail in this way). This is the predicted consequence of the stiffness-toughness trade-off of Section 2.3: widening the rib raises the plateau force until the lattice can no longer contain a crack. The failure marks the practical upper bound of the rib-stiffening strategy for Tough 1500 V1; beyond it, a tougher resin or a different rib cross-section is required.

5. Analytical Model

5.1 Updike's Rigid-Plastic Spherical Shell Analysis

The crushing of a thin-walled sphere between flat platens has been analysed as a travelling, or rolling, plastic hinge since Morris [18] showed that the plastic deformation of a pressed cylindrical shell localises in a narrow toroidal zone migrating outward as crushing proceeds. Updike [5] applied this idea to the sphere and derived the axial force for small inward deflection,

$$F = 2\pi\sqrt{3} \cdot \sigma_0 \cdot t^{3/2} \cdot \sqrt{\delta} \tag{2}$$

where σ_0 is the material flow stress, t the wall thickness and δ the plate displacement at the contact, with $2\pi\sqrt{3} \approx 10.9$. Two features matter. The force is independent of the sphere radius — a rolling hinge of a given wall thickness develops the same load whatever curvature it rides — so the plateau is set by thickness, not by how large the sphere is. And it is Updike's small-deflection result, derived for displacements between a few wall thicknesses and about one-tenth of the shell radius at the contact; De'Oliveira and Wierzbicki [6] later showed the same relation holds, to within a few percent, all the way to a crush of one shell radius. Integrating Eq. (2) gives the energy absorbed,

$$E = (4\pi\sqrt{3}/3) \cdot \sigma_0 \cdot t^{3/2} \cdot \delta^{3/2} \tag{3}$$

Gupta [8] characterised metallic spheres experimentally, identifying three stages: local flattening, axisymmetric inward dimpling about a rolling hinge, and — at larger compression — collapse into a pattern of non-axisymmetric circumferential lobes. In a metallic shell this lobe formation produces an initial load peak followed by a fluctuating, roughly constant mean. The ribbed lattice follows this metallic template and is discussed in Section 5.4.

5.2 Equivalent Shell Adaptation

The test articles are rib lattices, not uniform shells. To apply Updike's solution, an equivalent thickness is defined that produces the same plastic moment per unit length around the travelling hinge. For a U × V grid on a sphere of diameter D, the rib spacing at the equator is approximately

$$s = \pi \cdot D / N \tag{4}$$

with N = U = V = 20, giving s ≈ 9.42 mm for a 60 mm sphere. Each rib of width w (rib thickness) and depth h (wall thickness) has a fully plastic bending moment

$$M_p = \sigma_0 \cdot w \cdot h^2 / 4 \tag{5}$$

— the squared dependence on rib depth making the wall thickness a far stronger lever on plateau force than the rib width. Equating the moment per unit hinge length to that of a uniform shell of thickness teff:

$$t_{eff} = h \cdot \sqrt{(w / s)} \tag{6}$$

5.3 The Three-Mode Crush Response

The loading curve resolves into three sequential modes, illustrated in Figure 14 for both the reference 1.2 mm rib / 3.0 mm wall geometry and the thinner-walled 1.6 mm rib / 2.0 mm wall geometry across the velocity sweep. They occupy distinct ranges of crush depth and are governed by different mechanics, so the response is modelled mode by mode rather than by a single trend.

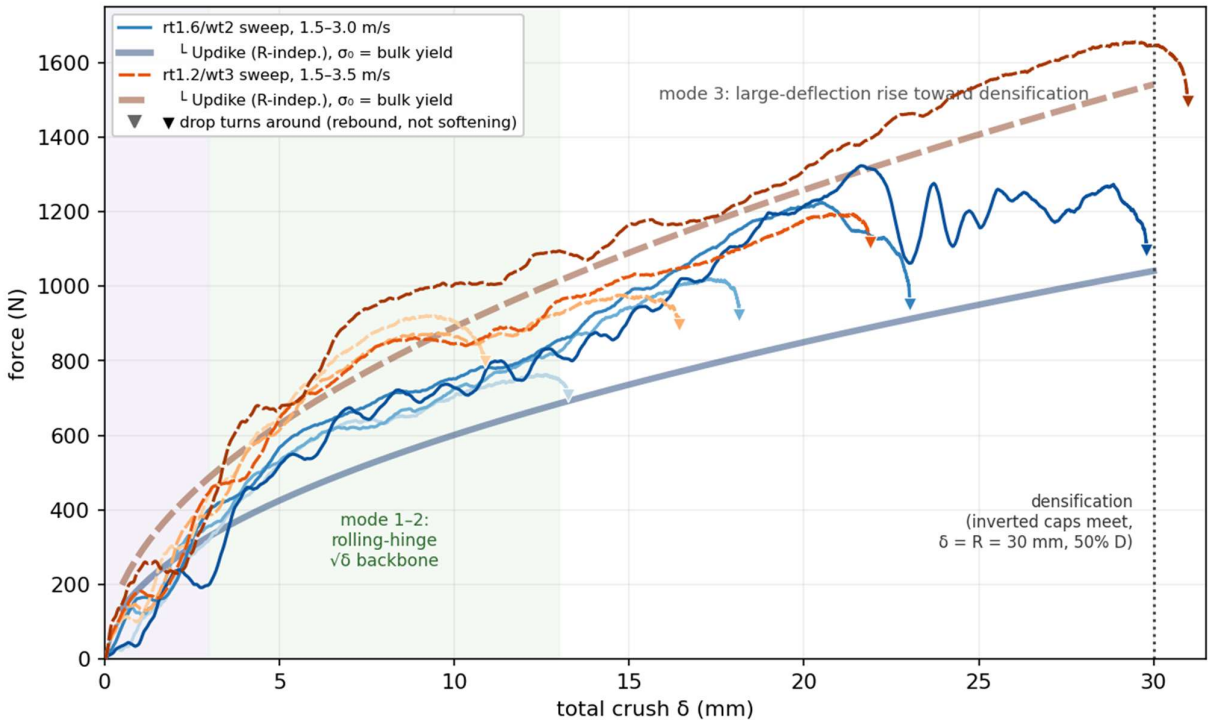


Figure 14 – Three-mode crush response for both geometries against total crush δ.

The 1.6 mm rib / 2.0 mm wall sweep (1.5–3.0 m/s, solid) and the 1.2 mm rib / 3.0 mm wall sweep (1.5–3.5 m/s, dashed) each collapse onto a single rolling-hinge backbone (Mode 2); the heavy faded curves are the radius-independent Updike prediction, Eq. (7), evaluated at the bulk yield stress with no fitted strength. Mode 1: both poles flatten, with snap-through troughs. Mode 3: beyond about 13 mm the load rises above the small-deflection √δ law toward densification. Triangles mark where each drop turns around as the impactor rebounds — not structural softening. Densification proper, where the inverted caps meet at the sphere centre, falls at δ = R = 30 mm, half the diameter (dotted line).

Mode 1 — pole flattening. The sphere is pressed at two poles, the upper against the impactor and the lower against the base. Both flatten, and each snaps through as its cap dimples inward, producing the irregular troughs in the first few millimetres of every trace. The phase is brief, spanning roughly the first five percent of diameter, and ends once both dimples have formed.

Mode 2 — rolling-hinge backbone. A plastic hinge then travels outward around each dimple — the rolling hinge of Section 5.1 — and the load follows Updike's radius-independent √δ law. The sphere is not a hemisphere: its two poles share the total crush, each indenting by δ/2, so the single-contact result applies at each pole and the full-sphere backbone is

$$F = 2\pi\sqrt{3} \cdot \sigma_0 \cdot t_{\text{eff}}^{3/2} \cdot \sqrt{(\delta/2)} \tag{7}$$

Across the velocity sweep this backbone is a single curve: the traces are coincident through the region, with a pooled power-law exponent of 0.49, confirming both the √δ form and that the rolling-hinge force is a property of the deformed geometry rather than of impact rate. Evaluated at the bulk yield stress — with no fitted strength — Eq. (7) reproduces the measured backbone of the reference geometry (Figure 14; the calibration is developed in Section 5.4). The backbone runs out near 13 mm of total crush, where the response turns up into Mode 3. This is the design-relevant plateau.

Mode 3 — large-deflection rise toward densification. Beyond about thirteen millimetres the measured load climbs above the small-deflection √δ backbone (Figure 14). This is not yet densification but the large-deflection regime of the same rolling hinge, in which the inverted caps deepen and the contact geometry stiffens; it is shared by every drop regardless of speed. Densification proper — the inverted caps meeting at the sphere centre — follows from the dimple kinematics: each cap centre travels inward at twice the plate rate, so the caps coincide when the total crush equals the sphere radius, δ = R = 30 mm, one half of the diameter. The decline at the end of each individual trace is not structural softening but rebound: the impactor reaches its turnaround and reverses, while a faster drop carrying more kinetic energy sails through the same depths under sustained load — the 3.0 m/s drop holds about 1.3 kN out to 28 mm, well past where the slower drops have already reversed. Densification bounds the usable stroke and sets the peak g-loading; it is the mode the graded-array concept of Section 8 is intended to defer.

5.4 Effective Strength and Transferability

The mode-2 backbone calibrates the effective flow stress σ_0. Fitted to the radius-independent law of Eq. (7) on the per-pole indentation, $\sigma_0 \approx 33$ MPa for the reference 1.2 mm rib / 3.0 mm wall geometry — equal, within the scatter, to the bulk yield of the printed resin. The rolling hinge therefore develops the full material strength. The low plateau force is instead geometric: through Eq. (6) the open lattice maps to a thin effective shell — about 1.1 mm here against the 3 mm structural wall — and because force grows as the three-halves power of effective thickness, a continuous shell of the full 3 mm wall at the same yield would develop nearly five times the force, exceeding the cargo g-limit. The lattice buys a low, controllable plateau by presenting a thin effective wall, not by working its material below yield. The reduced specific energy absorption is a favourable trade for airdrop, where limiting peak force governs, and the same geometric principle underpins metallic honeycomb crash structures.

Four geometries were swept to densification — 1.2 mm ribs on 3 and 4 mm walls, and 1.6 mm ribs on 2 and 3 mm walls; a 0.8 mm rib series was discarded, the displacements needed to reach peak force having tripped the Instron bump stops. Calibrated σ_0 sits near bulk yield for every geometry, the 1.6 mm rib / 2.0 mm wall lattice returning $\sigma_0 \approx 40$ MPa against ≈ 33 MPa for the reference 1.2 mm rib / 3.0 mm wall — the thinner-walled article a little above yield, the reference essentially at it. Through Eqs. (6) and (7) the backbone force scales as the three-halves power of wall thickness and the three-quarters power of rib width, so the wall is the stronger lever; completing that scaling across all four geometries awaits the backbone fits of the 4 mm wall and 1.6 mm rib / 3 mm wall articles.

Finally, the time to reach the plateau is approximately constant with velocity within each geometry — 6 to 12 ms from first contact across all four (Figures 10–13) — and shortens modestly with lattice stiffness, since a stiffer lattice carries more force, decelerates the impactor sooner, and arrests it at a shallower depth and earlier time.

6. Damping Characteristics

6.1 Definitions and Method

A crushing structure divides the absorbed energy into an irreversibly dissipated part and a recoverable elastic part returned to the payload as rebound; for a single-use dissipator the figure of merit is the fraction retained. The mechanism matters as much as the magnitude: a rate-independent absorber — structural hysteresis from progressive rib buckling and the travelling hinge — possesses a single force-displacement backbone F(δ) invariant with impact velocity, so one characterisation predicts the entire impact envelope, whereas a viscous absorber must be characterised at rate.

All energy quantities are evaluated in the displacement domain. The dissipated energy is the area enclosed by the force-displacement loop,

$$\Delta W = \oint F \, d\delta \tag{8}$$

and the specific damping capacity [19] is the ratio of dissipated to input work over the loading stroke,

$$\psi = \Delta W / W_{in}, \quad W_{in} = \int_0^{\delta max} F \, d\delta \tag{9}$$

with equivalent loss factor $\eta = \psi/2\pi$ and coefficient of restitution $e = v_{sep}/v_0$, related by $\psi \approx 1 - e^2$.

Velocity sweeps were run at a constant 5.4 kg drop mass: 1.5–3.0 m/s for the 1.6 mm rib / 2.0 mm wall geometry (UV_E) and 1.5–3.5 m/s for the 1.2 mm rib / 3.0 mm wall geometry (UV_A). Force was recorded at 1 MHz; striker displacement was measured independently by the optoNCDT 2300-50 and agreed with the force-integrated channel to 0.3 mm RMS (UV_E) and 0.4–0.9 mm RMS across four of five velocities (UV_A), with peak strokes within approximately 1 mm; the validated integrated channel is used where laser coverage is incomplete. The damping mechanism is identified by a fixed-penetration rate test: at a given penetration δ* the structure presents the same deformed geometry at a different local velocity in each test, so the loading force at δ* (averaged over ±0.75 mm to suppress rib-buckling noise) regressed against local velocity yields a slope of zero for rate-independent dissipation, or a viscous coefficient c such that $F(\delta, \dot{\delta}) \approx F0(\delta) + c \cdot \dot{\delta}$.

6.2 Tough 1500 V1 Characteristics

For the 1.6 mm rib / 2.0 mm wall geometry (Figure 15) the loading curves from all four velocities collapse onto a single backbone and the fixed-penetration slopes scatter about zero: dissipation is rate-independent, attributable to progressive plastic buckling of the ribs. A lumped viscoelastic fit $F = k\delta + c\dot{\delta}$ fails entirely ($R^2 = 0.09$); the dissipative force instead grows with crush depth, from approximately 260 N at 6 mm to 600 N near full stroke. The energy partition makes the mechanism explicit: the elastic return is approximately constant at 3 J — the bounded elastic capacity of the shell — while the dissipated energy grows with stroke (4.0, 8.1, 14.0 and 22.7 J at 1.5–3.0 m/s), so ψ rises from 0.59 to 0.89 and e falls from 0.58 to 0.29 across the sweep. At 3.0 m/s the laser-measured loop gives $W_{in} = 25.4$ J, $\Delta W = 22.7$ J and $\psi = 0.89$ ($\eta \approx 0.14$).

The 1.2 mm rib / 3.0 mm wall geometry departs in one respect (Figure 16): its loading curves fan weakly upward with speed and the fixed-penetration slopes are consistently positive (+43 to +60 N·s/m, $R^2 = 0.2$–0.5), a viscous contribution of roughly 10–15% of the loading force. With a thicker wall and lighter ribs this geometry deforms proportionally more by shell bending than by plastic rib collapse, so the photopolymer's intrinsic viscoelasticity becomes measurable. The energy trends mirror the stiffer-ribbed geometry — ψ rising from 0.50 to 0.86, e falling from 0.69 to 0.40, elastic return plateauing at 3–6 J — with a minority of the ψ trend attributable to rate. These fixed-penetration results are the basis of the kinematic interpretation of the velocity trend given in Section 5.4.

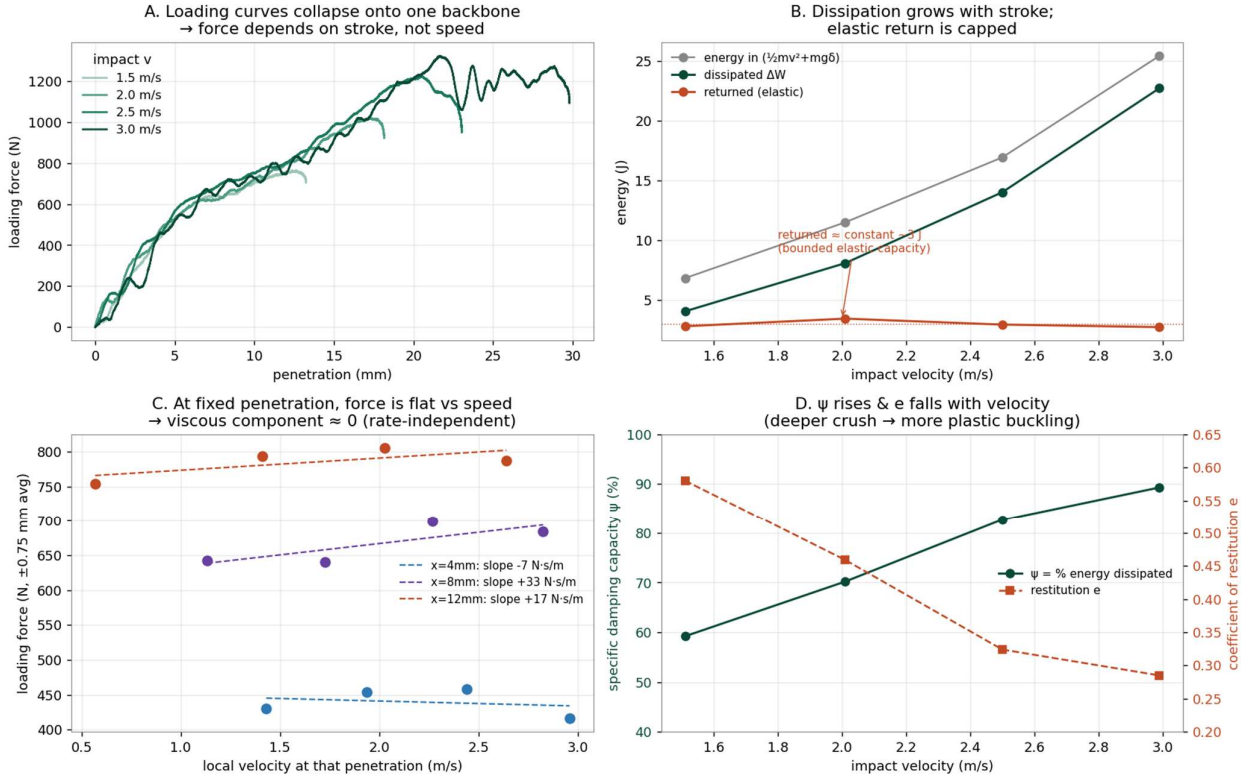


Figure 15 – Damping characterisation of the 1.6 mm rib / 2.0 mm wall geometry

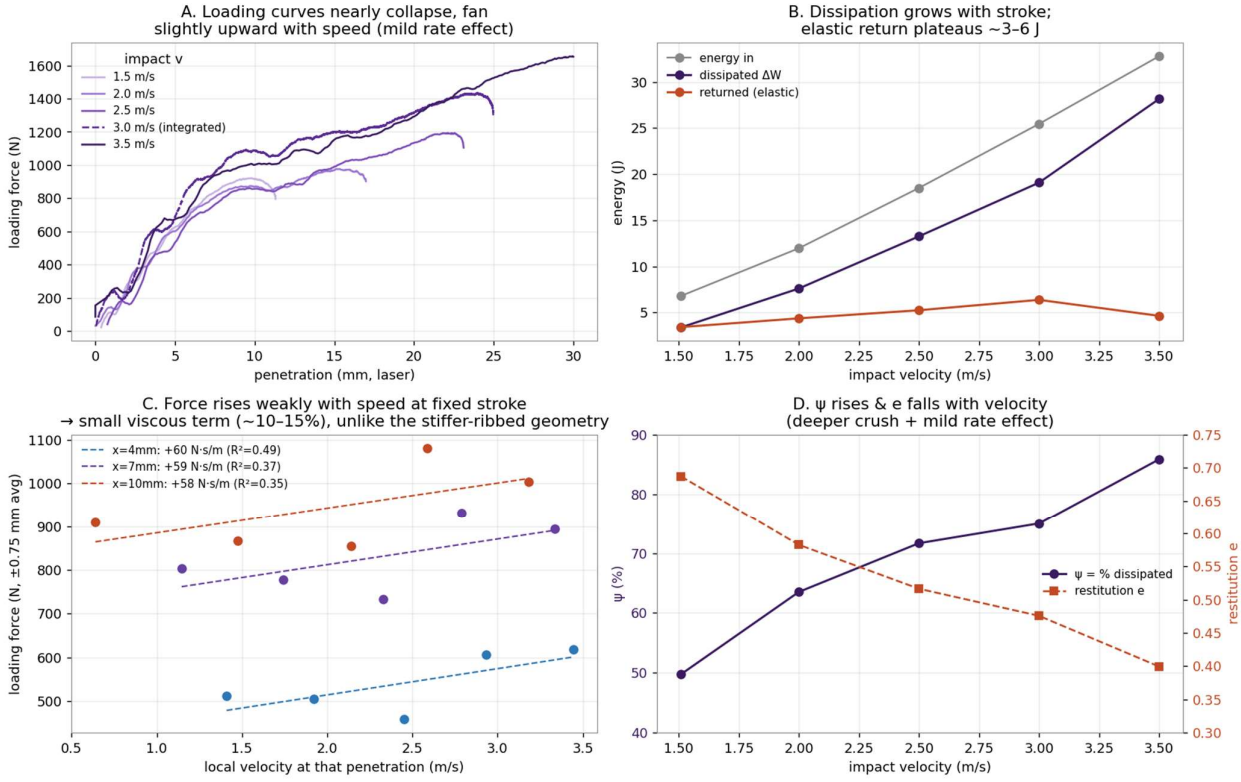


Figure 16 – Damping characterisation of the 1.2 mm rib / 3.0 mm wall geometry

6.3 Implications

Three conclusions follow. First, the slow post-impact recovery reflects not viscous damping but a structure that has expended its plastic capacity and retains only a small elastic reserve. Second, rate-independence confers design predictability: the measured backbone, with an energy balance, predicts peak force, stroke and g-loading for any payload mass and impact velocity within the envelope, without retesting at rate — a property shared with paper honeycomb, whose 3.0 m/s baseline returned approximately 2% of the input energy ($e \approx 0.10$, $\psi \approx 0.98$), the benchmark for a fully plastic dissipator. Third, geometry partitions the mechanism: increasing rib participation (thinner wall, thicker ribs) drives the response toward purely plastic, low-restitution behaviour, while shell-dominated variants trade dissipation for compliance and acquire mild rate sensitivity. Damping in these structures is therefore a design variable, set by the allocation of deformation between ribs and shell, rather than a fixed material property. The sweeps comprised single articles per velocity; the variance of ψ and of the fixed-penetration slopes across nominally identical articles remains to be quantified.

7. Discussion

Four findings are of practical significance for cargo airdrop. First, the single thin-walled sphere produces a force-time profile favourable relative to EDM: no initial peak and a sustained near-constant plateau, the post-plateau roll-off reflecting the impactor decelerating to rest rather than decaying capacity — constant force, constant g-loading, the ideal deceleration profile. Second, the wall thickness sets the plastic moment of each rib through a squared dependence while the rib thickness scales the local buckling resistance: two independent design levers — one for the velocity envelope and one for the g-loading — unavailable in conventional EDM. Third, the concentric configuration is not validated by dynamic testing; the loss of the rolling hinge at the sphere-on-sphere contact produces no advantage over a single-wall sphere of equivalent mass. Fourth, the rib geometry is also the fracture-management strategy: the rib width lies below the critical thickness for plane strain fracture in Tough 1500 V1 and the open lattice generally arrests cracking within one or two ribs, with the catastrophic failure of the stiffest geometry marking the practical upper bound of rib stiffening.

The damping characterisation adds a system-level property. The Tough 1500 V1 lattices are rate-independent dissipators: a single characterisation predicts the response across the impact envelope, and the rolling-hinge plateau force — the force delivered to the payload — is essentially velocity-invariant, with the velocity-sensitive part of the response confined to how deeply a faster impact crushes into densification rather than to any rate stiffening. The energy partition is equally consequential: the elastic energy returned to the payload is bounded (approximately 3–6 J across all Tough 1500 tests) while dissipation grows with stroke, so the specific damping capacity improves with impact severity, reaching $\psi \approx 0.9$ near the densification limit. The corresponding restitution ($e \approx 0.3$–0.4 at design-relevant velocities, against approximately 0.1 for crushed EDM) implies a modest rebound: the slow recovery returns energy as a low separation velocity rather than a ballistic relaunch, though asymmetric recovery across an array could contribute to tipping and should be assessed.

The efficiency reckoning against EDM must be made in the displacement domain. Defining a fill factor as the product of crush force efficiency (mean over peak force across the loading stroke) and stroke fraction (usable stroke over structure height), the ideal absorber — a rectangular force-displacement profile at the allowable peak force — scores unity. The sphere's geometric densification at or before approximately 50% of diameter — the rolling-hinge completion limit, with stiffer geometries densifying earlier — caps its stroke fraction below the approximately 70% available to a honeycomb stack, while its rising force profile reaches the force budget only late in the stroke. A single sphere therefore cannot match an ideally sized honeycomb per unit height, even at high crush force efficiency. Its compensating advantages are the absence of an initiation spike with the associated low jerk and a continuously tuneable design space; whether an engineered array can close the fill-factor gap while retaining these advantages motivates the future work below.

8. Conclusion and Future Work

This paper has characterised additively manufactured ribbed thin-walled spheres as candidate energy dissipators for cargo airdrop. Drop testing demonstrates a force profile with no initiation peak and a sustained plateau produced by a rolling plastic hinge; the crush response resolves into three modes — pole flattening, a velocity-invariant rolling-hinge backbone following Updike's radius-independent $\sqrt{\delta}$ law (the full sphere pressed at both poles, each taking half the crush; calibrated against the law with no fitted strength), and a large-deflection rise toward densification, the inverted caps meeting at half the diameter — with the lattice undergoing the metallic shell's inward dimpling. The dominant dissipation mechanism is rate-independent structural hysteresis with specific damping capacity rising to approximately 0.9. Finally, the concentric configuration is empirically rejected in favour of single-wall arrays. The single sphere concedes the per-height energy contest to honeycomb through earlier densification, which focuses future effort at the array level. The immediate priorities are:

- addressing the fill factor through a graded array synthesising a pseudo-plateau. As the Tough 1500 lattice is rate-independent, the response of an array is expected to approximate the superposition of its members' measured force-displacement backbones. A superposition model built from the single-sphere backbones characterised in this work will be used to design arrays of mixed wall and rib thickness whose individual densification strokes are staggered: softer members initiate load early, stiffer members engage progressively as the softer approach densification, flattening the aggregate force-displacement curve and softening the approach to bottoming. Drop-tower testing of small parallel and series (interlayer-plated) arrays will quantify where superposition breaks down, and the best graded recipe will be benchmarked against an equal-height, equal-footprint honeycomb block at matched energy — including at 15–30° of platen obliquity, where the omnidirectional sphere is expected to hold its performance;
- optimising the geometry to flatten the polar regions, that provide little energy dissipation but consume 10% of the stroke;
- refinement of the LS-DYNA model to incorporate the curved reaction surface effect identified in Section 4.1 and the rate-independent backbone established in Section 6, and re-baselining of the FEA against the empirical traces; and
- a sizing study for a clustered single-wall sphere array on a 1118 × 1118 × 381 mm container airdrop platform with a 998 kg payload, including the role of interlayer plates in homogenising the load between layers.

9. Contact Author Email Address

mailto: andrew.lloyd@sydney.edu.au

10. Copyright Statement

The authors confirm that they, and/or their company or organization, hold copyright on all of the original material included in this paper. The authors also confirm that they have obtained permission, from the copyright holder of any third party material included in this paper, to publish it as part of their paper. The authors confirm that they give permission, or have obtained permission from the copyright holder of this paper, for the publication and distribution of this paper as part of the ICAS proceedings or as individual off-prints from the proceedings.

References

[1] Air Movements Training and Development Unit, *Aerial Delivery Design Handbook*, Administrative Officer AMTDU, Richmond, NSW, Australia, 2007.

[2] Department of Defense. Honeycomb Material, Cushioning, Paper. MIL-PRF-9884F, Natick, MA, 1997.

[3] Department of Defence. AAP7279.001-1-1 Air Drop of Material General – Container Rigging and Associated Equipment, Sect. 1, Chap. 2, Richmond, NSW, Australia, 2012.

[4] Lloyd A and Wong K. A Novel Energy Dissipator for Airdrop; With Bespoke Geometry Enabled by Additive Manufacturing. *AIAA Aviation Forum and ASCEND 2024*. doi: 10.2514/6.2024-4518.

[5] Updike DP. On the large deformation of a rigid-plastic spherical shell compressed by a rigid plate. *Journal of Engineering for Industry*, Vol. 94, 1972, pp. 949–955.

[6] De'Oliveira JG and Wierzbicki T. Crushing analysis of rotationally symmetric plastic shells. *Journal of Strain Analysis*, Vol. 17, No. 4, 1982, pp. 229–236.

[7] Calladine CR. Analysis of large plastic deformations in shell structures. In: *Inelastic Behaviour of Plates and Shells*, Springer, 1986, pp. 69–101.

[8] Gupta NK and Easwara Prasad GL. Dynamic crushing of thin-walled spheres: an experimental study. *International Journal of Impact Engineering*, Vol. 35, 2008, pp. 1267–1285.

[9] Calladine CR and English RW. Strain-rate and inertia effects in the collapse of two types of energy-absorbing structure. *International Journal of Mechanical Sciences*, Vol. 26, Issues 11–12, 1984, pp. 689–701. doi: 10.1016/0020-7403(84)90021-3.

[10] Ligon-Auer SC, Schwentenwein M, Gorsche C, Stampfl J and Liska R. Toughening of photo-curable polymer networks: a review. *Polymer Chemistry*, Vol. 7, 2016, pp. 257–286. doi: 10.1039/C5PY01631B.

[11] Idrees M, Yoon H, Palmese GR and Alvarez NJ. Engineering Toughness in a Brittle Vinyl Ester Resin Using Urethane Acrylate for Additive Manufacturing. *Polymers*, Vol. 15, 2023, 3501. doi: 10.3390/polym15173501.

[12] Anderson TL. *Fracture Mechanics: Fundamentals and Applications*, 4th ed. CRC Press, Boca Raton, 2017.

[13] Formlabs. Methods for Measuring Toughness. Formlabs Blog, 2025. Available at: formlabs.com/blog/measuring-toughness-methods/. Accessed May 2026.

[14] Yudha NK, Muwaffaq AM, Putro AJN, Wu YC, Widagdo D, Darmanto S, Santos GNC and Muflikhun MA. Crack in stereolithography: material and surface characteristics based on DIC. *Next Research*, 2025, 100323. doi: 10.1016/j.nexres.2025.100323.

[15] Quagliato L, Kim SY and Ryu SC. Quasi-ductile to brittle transitional behavior and material properties gradient for additively manufactured SLA acrylate. *Materials Letters*, Vol. 329, 2022, 133121. doi: 10.1016/j.matlet.2022.133121.

[16] Richeton J, Ahzi S, Vecchio KS, Jiang FC and Adharapurapu RR. Influence of temperature and strain rate on the mechanical behavior of three amorphous polymers. *International Journal of Solids and Structures*, Vol. 43, 2006, pp. 2318–2335.

[17] Roland CM. High Strain Rate Mechanics of Polymers: A Review. *Journal of Dynamic Behavior of Materials*, Vol. 2, 2016, pp. 208–223. doi: 10.1007/s40870-016-0052-8.

[18] Morris AJ. The local strength of a thin spherical shell loaded radially through a rigid boss. In: Berman I (ed.), *Proceedings of the First International Conference on Pressure Vessel Technology, Part 1*, ASME, 1969, pp. 35–44.

[19] Lazan BJ. *Damping of Materials and Members in Structural Mechanics*, Pergamon Press, Oxford, 1968.